1999

Mathematical Modeling of Electrochemical Capacitors

Venkat Srinivasan
University of South Carolina - Columbia

John W. Weidner
University of South Carolina - Columbia, weidner@engr.sc.edu

Publication Info

Journal of the Electrochemical Society, 1999, pages 1650-1658.

Publisher's link: http://dx.doi.org/10.1149/1.1391821
DOI: 10.1149/1.1391821

Journal of The Electrochemical Society, **146** (5) 1650-1658 (1999)
S0013-4651(98)08-081-1 CCC: $7.00

Mathematical Modeling of Electrochemical Capacitors

Venkat Srinivasan* and John W. Weidner,z**

Department of Chemical Engineering, University of South Carolina, Columbia, South Carolina 29208, USA

Analytic solutions to the mathematical model of an electrochemical capacitor (EC) are used to study cell performance under two types of operating conditions: (*i*) constant current and (*ii*) electrochemical impedance spectroscopy. The analytic solution under constant-current operation is used to investigate the relative importance of ionic resistance in the separator, and ionic and electronic resistances in the porous electrode in the design and operation of an EC. Model results are presented that show the trade-off between energy and power density, as the physical properties of the cell components are varied (e.g., electrode thickness). The analytic solution is also used to study the effect of cell design and operation on the heat generation during constant-current cycling. The impedance model is presented as an alternative to equivalent-circuit models for data analysis. The analytic solution can be used to gain a physical understanding of the various processes that occur in an EC.

Manuscript submitted August 24, 1998; revised manuscript received November 19, 1998.

Due to the high-rate capability of electrochemical capacitors (EC), they are considered excellent candidates for use in high-power applications such as load leveling the power sources in electric vehicles.[1-3] Electrochemical capacitors having large capacitance per gram of active material are of two types,[1] (*i*) double-layer capacitors and (*ii*) pseudocapacitors. The energy in the former device is stored across the double layer formed at the interface between an electronically conducting substrate and the electrolyte. The capacitance of a double layer is typically in the range of 10 to 40 μF per cm^2 of surface area.[4] Therefore, to achieve the requisite energy densities, high-surface-area materials such as activated carbon are used.[5] In contrast, pseudocapacitors are based on faradaic reactions that exhibit a current-voltage response similar to a capacitor. Examples of systems that exhibit faradaic pseudocapacitance are underpotential deposition of H or Pb in monolayers on noble metals and redox reactions of microporous transition metal hydrous oxides such as RuO_2 [1] and NiO. [6,7]

To produce cost-effective materials with the desired electrochemical performance, a systematic approach is needed to relate process conditions to electrochemical characteristics. Such a systematic approach can be aided by mathematical models for understanding the relationship between electrode structure (e.g., porosity, capacitance, surface area, and thickness) and performance (e.g., energy and power density). The objective of this paper is to use mathematical models to (*i*) develop a relationship between the physical properties of the cell components and the energy and power density of the device; (*ii*) gauge the importance of thermal effects on the performance of these devices; and (*iii*) develop an electroanalytical tool to probe fundamental properties of new materials in advanced devices. Tasks (*i*) and (*ii*) were achieved by solving the governing equation under constant-current operation, while task (*iii*) was achieved by simulating electrochemical impedance spectroscopy. This paper modifies the constant-current model developed by Farahmandi[8] for calculating the energy and power densities of the cell as a function of design parameters and operating conditions. The model has also been used to simulate the temperature rise in the cell during constant-current cycling.

There are numerous models dealing with the double-layer formation in porous electrodes in the literature. These models can be divided into two categories: (*i*) models used to simulate the charging of the double layer[9-13] and (*ii*) models used to simulate the performance of electrochemical capacitors.[8,14,15] Posey and Morozumi[9] presented macroscopic equations to describe the charging of the double layer at constant current and constant potential and subsequently these equations were used by other researchers to analyze the double-layer charging phenomena.[10-13] Models to simulate the performance of an electrochemical capacitor were initiated by Pillay and Newman,[14] who looked at the constant-current operation of the cell to analyze the effect of the oxygen and hydrogen evolution reactions. Using Tafel kinetics, the authors conclude that the two side reactions result in considerable efficiency losses during early cycles even when operating the cell within the thermodynamic stability window of the electrolyte. Farahmandi[8] looked at the effect of the ionic and electronic resistances on the galvanostatic charging of an electrochemical capacitor and discussed methods to determine the initial resistance and the steady-state resistance using the shape of the voltage profile. This work, however, does not relate the physical properties of the cell components to the energy and power density of the device. Nor was the model used to study the effect of cell design and operation on the heat generation during constant-current cycling. Miller[15] used equivalent circuits rather than porous-electrode theory to describe the electrochemical impedance spectroscopy of a device. In this work, we take advantage of the porous-electrode model developed for constant-current cycling to simulate electrochemical impedance in an EC.

Model Development

Assumptions.—A schematic diagram of the double-layer capacitor cell modeled here is shown in Fig. 1. The cell consists of two identical porous electrodes with a separator between them and electrolyte throughout. The assumptions made in developing the model are summarized as 1, All faradaic processes result in a current-voltage profile similar to that of a capacitor. 2, The electrolyte concentration is uniform throughout. 3, Ohmic losses are the dominating phenomenon behind the heating effect. 4, The temperature is constant throughout the cell, but it changes with time. 5, The capacitance is constant over the voltage window of operation. 6, The physical properties of the device (e.g., conductivity and capacitance) do not vary during a charge (or discharge).

Governing equations.—In the absence of concentration variations, the current density in the matrix and solution phases can be expressed by Ohm's law as

$$i_1 = -\sigma \frac{\partial(\phi_1)}{\partial x} \quad [1]$$

$$i_2 = -\kappa \frac{\partial(\phi_2)}{\partial x} \quad [2]$$

The conservation of charge leads to the following two equations

$$I = i_1 + i_2 \quad [3]$$

$$\frac{\partial i_1}{\partial x} = -\frac{\partial i_2}{\partial x} = a i_n \quad [4]$$

* Electrochemical Society Student Member.
** Electrochemical Society Active Member.
z E-mail: weidner@engr.sc.edu

S0013-4651(98)08-081-1 CCC: $7.00

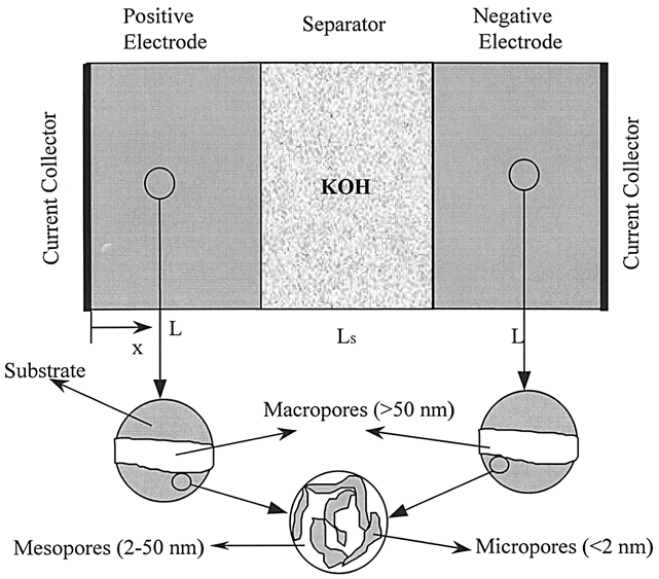

Figure 1. Schematic diagram of the electrochemical capacitor (EC) considered here. The electrode thickness is L and the separator thickness is L_s. The current collector and the electrode/separator interface are at $x = 0$ and $x = \mathrm{L}$, respectively.

Due to assumption 1, the relationship between the interfacial potential difference and the transfer current is given by

$$i_n = -C\frac{\partial(\phi_1 - \phi_2)}{\partial t} \qquad [5]$$

Equations 1-5 can be combined and converted to dimensionless form to yield

$$\frac{\partial^2\eta^*}{\partial\xi^2} = \frac{\partial\eta^*}{\partial\tau} \qquad [6]$$

where η^* is the dimensionless overpotential.

The overpotential is initially set to zero throughout the electrode, thus leading to the solution of Eq. 6 in the Laplace domain as

$$\overline{\eta}^* = C_1\cosh(\sqrt{s}\xi) + C_2\sinh(\sqrt{s}\xi) \qquad [7]$$

where C_1 and C_2 are constants that are evaluated depending on the boundary conditions.

Equations 1-3 can be combined to yield the solution-phase current in terms of the overpotential as

$$\frac{i_2}{I} = \frac{\gamma}{(1+\gamma)} + \frac{1}{I^*}\frac{\partial\eta}{\partial\xi} \qquad [8]$$

where I^* is the dimensionless cell current. Using the fact that the cell current is equal to the matrix phase and solution phase currents at $x = 0$ and $x = L$, respectively, Eq. 8 can be written for the two boundary conditions as

$$\xi = 0 \qquad \frac{\partial\eta^*}{\partial\xi} = -I^*(t)\frac{\gamma}{(1+\gamma)} \qquad [9a]$$

$$\xi = 1 \qquad \frac{\partial\eta^*}{\partial\xi} = I^*(t)\frac{1}{(1+\gamma)} \qquad [9b]$$

The dimensionless current, I^*, can vary with time if the cell current changes (e.g., electrochemical impedance spectroscopy). Equations 9a and b can be used to evaluate the constants C_1 and C_2 in Eq. 7 to yield the overpotential in the Laplace domain as

$$\overline{\eta}^* = \frac{\bar{I}^*\cosh\left(\sqrt{s}\xi\right) + \bar{I}^*\gamma\cosh\left[\sqrt{s}(1-\xi)\right]}{\sqrt{s}(1+\gamma)\sinh\left(\sqrt{s}\right)} \qquad [10]$$

Differentiating Eq. 10, substituting that result into Eq. 8, and solving for the solution current yields

$$\frac{\bar{i}_2}{\bar{I}} = \frac{\gamma}{(1+\gamma)} + \frac{\gamma\sinh\left(\sqrt{s}\xi\right) - \sinh\left[\sqrt{s}(1-\xi)\right]}{(1+\gamma)\sinh\left(\sqrt{s}\right)} \qquad [11]$$

Equation 11 can be substituted into Eq. 2 and integrated to yield the change in potential across the porous electrode as

$$\frac{\overline{\phi}_2\big|_{\xi=0} - \overline{\phi}_2\big|_{\xi=1}}{V_o} = \frac{\bar{I}^*\left[1-\cosh\left(\sqrt{s}\right)\right](\gamma-1)}{(\gamma+1)^2\sqrt{s}\sinh\left(\sqrt{s}\right)} + \frac{\bar{I}^*\gamma}{(\gamma+1)^2} \qquad [12]$$

The voltage of a cell consisting of two porous electrodes with a separator between them can be evaluated using

$$\begin{aligned} V_{cell} &= 2V_o - 2\left(\phi_1\big|_{\xi=0} - \phi_2\big|_{\xi=1}\right) - \frac{IL_s}{\kappa_s} \\ &= 2V_o - 2\left[\left(\phi_2\big|_{\xi=0} - \phi_2\big|_{\xi=1}\right)\right. \\ &\qquad \left. + \left(\phi_1\big|_{\xi=0} - \phi_2\big|_{\xi=0}\right)\right] - \frac{IL_s}{\kappa_s} \\ &= 2V_o - 2\left[\left(\phi_2\big|_{\xi=0} - \phi_2\big|_{\xi=1}\right) + \eta\big|_{\xi=0}\right] - \frac{IL_s}{\kappa_s} \end{aligned} \qquad [13]$$

The first term accounts for the initial voltage of the cell at the start of discharge. The terms in the square brackets give the potential drop across each of the electrodes. The third term accounts for the potential drop across the separator.

Substituting Eq. 10 and 12 into Eq. 13 yields the voltage in the Laplace domain as

$$\overline{V}^* = \frac{\overline{V}_{cell}}{2V_o} = 1 - \frac{2\gamma\bar{I}^*}{(1+\gamma)^2\sqrt{s}\sinh\left(\sqrt{s}\right)} - \frac{(1+\gamma^2)\bar{I}^*}{(1+\gamma)^2}\frac{\coth\left(\sqrt{s}\right)}{\sqrt{s}} - \frac{\gamma\bar{I}^*}{(1+\gamma)^2} - \frac{\beta\bar{I}^*}{2} \qquad [14]$$

Cell voltage and local double-layer current for constant current discharge.—For a constant-current discharge, the applied current is known, and therefore I^* is a known constant. Equation 14 can be solved by inverting it to the time domain to yield

$$V^* = 1 - I^*\left(\frac{1}{3} + \tau - 2\sum_{n=1}^{\infty}\frac{\left(\frac{(-1)^n\gamma}{(\gamma+1)} + \frac{1}{(\gamma+1)}\right)^2\exp(-n^2\pi^2\tau)}{n^2\pi^2}\right) - \frac{\beta I^*}{2} \qquad [15]$$

where V^* is a function of the independent variable τ, and three dimensionless parameters: I^*, the dimensionless current; β, the ratio of the separator to electrode resistance; and γ, the ratio of the solution and matrix phase conductivities.

Equation 10 can be inverted to the time domain to give the overpotential throughout each electrode as

$$\eta^* = I^*\tau + \frac{I^*(3\xi^2-1)}{6(1+\gamma)} + \frac{I^*\gamma(3\xi^2+2-6\xi)}{6(1+\gamma)} - \frac{2I^*}{\pi^2(1+\gamma)}\sum_{n=1}^{\infty}\left[\frac{(-1)^n+\gamma}{n^2}\right]\cos(n\pi\xi)\exp(-n^2\pi^2\tau) \qquad [16]$$

S0013-4651(98)08-081-1 CCC: $7.00

The double-layer discharging current can be evaluated by taking the time derivative of the overpotential (Eq. 16) and substituting the resultant expression into Eq. 5 to yield

$$j_n^* = -\frac{i_n aL}{I}$$

$$= 1 + \frac{2}{(1+\gamma)} \sum_{n=1}^{\infty} \left[(-1)^n + \gamma\right] \cos(n\pi\xi) \exp(-n^2\pi^2\tau) \quad [17]$$

Energy balance for constant current discharge.—The deviation of the voltage of the porous capacitor from that of an ideal capacitor due to ohmic losses leads to heat generation. With the assumption that the temperature rise is uniform throughout the cell, the energy balance for the cell can be expressed in dimensional form as

$$mC_P \frac{dT}{dt} + hA_C(T - T_S) = IV_{dev} \quad [18]$$

The specific heat capacity of the cell was estimated from the individual heat capacities using

$$C_P = \frac{(2LA\rho_{electrode}c_{P,carbon} + L_S A\rho_{separator}c_{P,separator} + 2\epsilon_O LA\rho_{electrolyte}c_{P,KOH} + \epsilon_S LA\rho_{electrolyte}c_{P,KOH})}{m} \quad [19]$$

The voltage deviation in Eq. 18 is obtained from Eq. 15 as

$$\frac{V_{dev}}{V_O} = \frac{V_{ideal} - V_{cell}}{V_O}$$

$$= \frac{2I^*}{3} - 4I^* \sum_{n=1}^{\infty} \frac{\left(\frac{(-1)^n\gamma}{(\gamma+1)} + \frac{1}{(\gamma+1)}\right)^2 \exp(-n^2\pi^2\tau)}{n^2\pi^2} + \beta I^* \quad [20]$$

The capacitance and conductivities of the solution and the electrode material are assumed to be constant during a half cycle. Therefore, Eq. 20 is substituted into Eq. 18, and the resultant expression is integrated to give

$$\frac{T_k}{T_{k-1}} = \left(\frac{2I^*\lambda}{3h^*} + \frac{\beta I^*\lambda}{2h^*} + \frac{\lambda}{2}\right)\left(1 - \frac{1}{\exp\left(\frac{\tau_c I^*\lambda}{h^* C_P^*}\right)}\right) + \frac{1}{\exp\left(\frac{\tau_c I^*\lambda}{h^* C_P^*}\right)} - 4\frac{I^{*2}}{C_P^*} \sum_{n=1}^{\infty} \frac{\left(\frac{(-1)^n\gamma}{(\gamma+1)} + \frac{1}{(\gamma+1)}\right)^2 \left(\exp\left(-n^2\pi^2\tau_c\right) - \frac{1}{\exp\left(\frac{\tau_c I^*\lambda}{h^* C_P^*}\right)}\right)}{n^2\pi^2\left(-n^2\pi^2 + \frac{\tau_c I^*\lambda}{h^* C_P^*}\right)} \quad [21]$$

where k represents temperature at the end of the kth half cycle and τ_c is the time taken to reach the cutoff potential. In addition to the three dimensionless parameters that govern the cell voltage, namely, I^*, β, and γ, the temperature of the cell depends on h^*, the dimensionless external heat-transfer coefficient; C_P^*, the dimensionless specific heat capacity; and λ, the ratio of ambient temperature to the initial cell temperature. For simulation of the cell temperature on repeated charge/discharge cycling using Eq. 21, the cycle number, k, is the dependent variable.

To calculate the temperature rise during a half cycle, Eq. 15 is solved at a particular current to find the time taken to reach the cutoff voltage, τ_c. This cutoff time is substituted into Eq. 21 to find the temperature rise for that half cycle.

Impedance spectroscopy.—To simulate the impedance of the cell, a sinusoidal voltage perturbation is applied to the system and the current response is measured. Since the cell current changes with time during an impedance experiment, I^* varies. In this case, Eq. 14 can be transformed from the Laplace domain to the frequency domain by substituting for the dimensionless Laplace operator, s, with a complex variable $p + j\omega^*$. Assuming that a small alternating voltage signal ($\leq$10 mV) does not perturb the system significantly from the steady state achieved prior to the start of the experiment, p can be set to zero. Replacing s with $j\omega^*$ in Eq. 14 yields the expression for the cell voltage in the frequency domain.

The impedance of the cell is evaluated by differentiating the voltage expression (i.e., Eq. 14) with respect to the current and replacing s with $j\omega^*$. In dimensionless form the impedance is defined as

$$Z^* = -2\frac{dV^*}{dI^*} = \frac{4\gamma}{(1+\gamma)^2\sqrt{j\omega^*}\sinh\left(\sqrt{j\omega^*}\right)} + \frac{2(1+\gamma^2)}{(1+\gamma)^2}\frac{\coth\left(\sqrt{j\omega^*}\right)}{\sqrt{j\omega^*}} + \frac{2\gamma}{(1+\gamma)^2} + \beta \quad [22]$$

To generate the Nyquist plot, Eq. 22 is rewritten in the following form

$$Z^*(\omega^*) = Re^*(\omega^*) + jIm^*(\omega^*) \quad [23]$$

to yield

$$Re^* = \frac{(1+\gamma^2)}{(1+\gamma)^2\omega^*}\left\{\frac{\sinh(\omega^*)\cosh(\omega^*) - \sin(\omega^*)\cos(\omega^*)}{\cosh^2(\omega^*) - \cos^2(\omega^*)}\right\} + 2\frac{\gamma}{(1+\gamma)^2\omega^*}\left\{\frac{\sinh(\omega^*)\cos(\omega^*) - \cosh^2(\omega^*)\sin(\omega^*)}{\cosh^2(\omega^*) - \cos^2(\omega^*)}\right\} + 2\frac{\gamma}{(1+\gamma)^2} + \beta \quad [24a]$$

$$Im^* = \frac{\left(1+\gamma^2\right)}{(1+\gamma)^2\omega^*}\left\{\frac{\sinh(\omega^*)\cosh(\omega^*) + \sin(\omega^*)\cos(\omega^*)}{\cosh^2(\omega^*) - \cos^2(\omega^*)}\right\} + 2\frac{\gamma}{(1+\gamma)^2\omega^*}\left\{\frac{\sinh(\omega^*)\cos(\omega^*) + \cosh(\omega^*)\sin(\omega^*)}{\cosh^2(\omega^*) - \cos^2(\omega^*)}\right\} \quad [24b]$$

The impedance of an electrochemical capacitor is a function of the dependent variable ω^*, the dimensionless frequency, and two dimensionless parameters: β, the ratio of external to internal resistance, and γ, the ratio of solution to matrix phase conductivity. When $\gamma = 0$, Eq. 24a and b collapse to Eq. 10a and b derived by Motupally et al.[16] for the impedance response of a diffusion-limited process.

Results and Discussion

Constant-current discharge.—Figure 2 shows dimensionless discharge curves generated from Eq. 15 for different values of the dimensionless current. The abscissa in Fig. 2 is the relative utiliza-

S0013-4651(98)08-081-1 CCC: $7.00

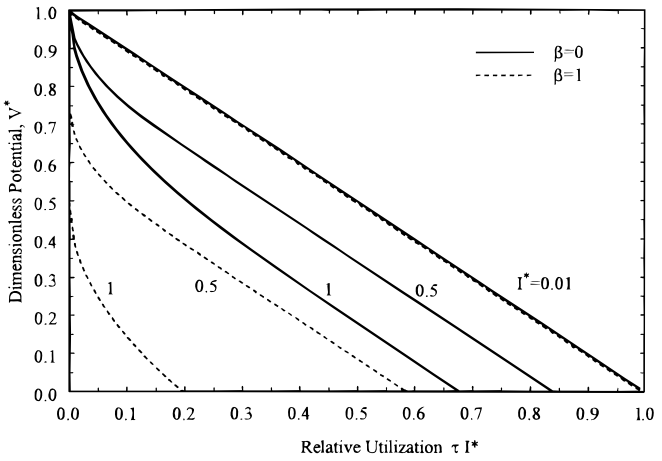

Figure 2. Normalized constant-current discharge curves as a function of the dimensionless current for an EC. The solid line corresponds to negligible separator resistance, and the dashed line for separator resistance equal to that of the electrode. The matrix phase conductivity is negligible relative to the electrolyte conductivity (i.e., $\gamma = 0$).

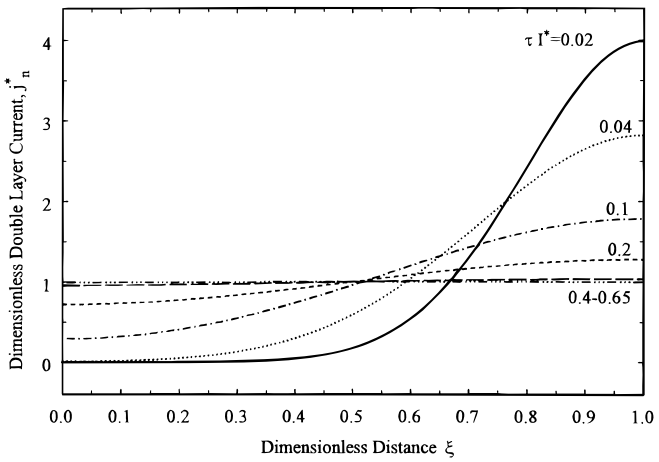

Figure 3. Double-layer current distribution through the positive electrode as a function of time during constant-current discharge of an EC for $I^* = 1.0$. The matrix phase conductivity is much greater than the solution (i.e., $\gamma = 0$). At $\gamma = \infty$ or at the negative electrode, the current distribution would be the mirror image of those shown here.

tion, τI^*. The value of τI^* represents the fraction of the available capacity extracted from the cell. The solid line corresponds to a negligible separator resistance (i.e., $\beta = 0$) and the dashed line corresponds to a separator resistance equal to that of the electrode (i.e., $\beta = 1$). The matrix-phase conductivity is negligible relative to the electrolyte conductivity (i.e., $\gamma = 0$) for all the curves. Figure 2 is characterized by three distinguishing features: (*i*) a sharp drop in voltage at the start of discharge for higher discharge rates; (*ii*) a straight-line portion for the rest of the discharge; and (*iii*) electrode utilization that decreases as the discharge rate increases. The sharp drop in voltage at the start of discharge is the result of a time constant for the double-layer current distribution to reach a steady state. Once the current distribution becomes uniform throughout the electrode, the discharge is characterized by a linear voltage decrease. In this portion, the slope of the line is that of an ideal capacitor (i.e., proportional to the current divided by the capacitance). As I^* or β increases, ohmic effects become significant, and the capacity extracted from the cell when it reaches 0 V is less than the maximum capacity.

The physical significance of the shape of the discharge curve shown in Fig. 2 can be seen by examining the limits of Eq. 15. At the start of discharge (i.e., $\tau = 0$), Eq. 15 can be expressed in dimensional form as

$$V_{\text{cell}}\big|_{t\to 0} = 2V_o - \frac{2IL}{(\kappa + \sigma)} - \frac{IL_s}{\kappa_s} \qquad [25]$$

In this limit the electrochemical capacitor behaves as if the separator resistance is in series with two parallel resistors, one for the matrix and the other for the solution.[8] Since the current takes the path of least resistance, the voltage drop across the parallel resistors is dictated by the resistance of the most conductive path. At long times, Eq. 15 reduces to a straight line of the form

$$V_{\text{cell}}\big|_{t\to\infty} = \left\{\frac{I}{aCL/2}\right\}t + \left\{2V_o - \frac{2}{3}\frac{IL(\kappa + \sigma)}{\kappa\sigma} - \frac{IL_s}{\kappa_s}\right\} \qquad [26]$$

Equation 26 corresponds to the voltage-time profile of an ideal capacitor with a voltage offset due to three resistors in series (i.e., separator, matrix, and solution). The intercept in Eq. 26 is consistent with the steady-state resistance determined by Farahmandi.[8]

The distribution of the double-layer current throughout the positive electrode at different discharge times is illustrated in Fig. 3. At the negative electrode or at $\gamma = \infty$, the current distribution is the mirror image of those shown in Fig. 3. The plot was generated using Eq. 17, for $I^* = 1.0$, $\beta = 0$, and $\gamma = 0$. At short times, the current distribution is very nonuniform with virtually none of the double-layer discharging at the current collector (i.e., $\xi = 0$). This profile is consistent with the voltage limit at $t \to 0$ (i.e., Eq. 25). At $\gamma = 0$ (i.e., $\sigma = \infty$), all the current goes through the matrix phase, and therefore the porous electrode does not contribute to the cell resistance. With increasing time, the distribution becomes uniform, and at $\tau I^* > 0.4$, the double-layer current is approximately equal to 1.0 throughout. This uniform current causes the porous electrode to behave like two resistors in series (see Eq. 26).

The nonuniform current distribution gives rise to the curvature in the cell voltage at the start of discharge. As the double-layer current distribution becomes uniform, the discharge profile reaches that of the ideal capacitor. The uniform current distribution, however, does not translate into a uniform potential distribution. The effect of appreciable ohmic resistance on the potential distribution with time can be seen in Fig. 4, where the overpotential is plotted with distance for increasing discharge times. The plot was generated using Eq. 16 for $I^* = 1.0$, $\beta = 0$, and $\gamma = 0$. As illustrated in Fig. 4, the potential distribution is nonuniform even for $\tau I^* > 0.4$. Only at low currents or low resistance (e.g., $I^* = 0.01$) is the overpotential uniform throughout the electrode. However, as indicated in Eq. 5, the local change in potential with time results in the double-layer current. The change in potential from $\tau I^* = 0.4$ to $\tau I^* = 0.65$ is approximately

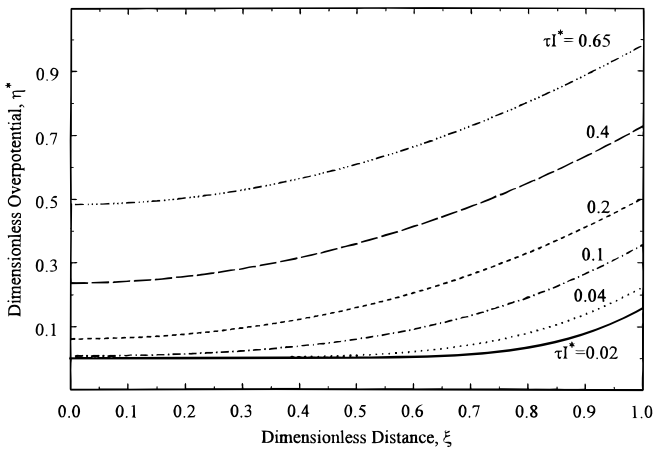

Figure 4. Overpotential distribution through the positive electrode as a function of time during constant-current discharge of an EC for $\gamma = 0$ and $I^* = 1.0$. At $\gamma = \infty$ or at the negative electrode, the overpotential distribution would be the mirror image of those shown here.

S0013-4651(98)08-081-1 CCC: $7.00

the same at the front of the electrode as at the back. Therefore, although the potential distribution remains nonuniform at long times, the current distribution is uniform. At short times, the change in potential is greater at the front (i.e., $\xi = 0$) than at the back, which leads to the nonuniform current distribution seen in Fig. 3.

In contrast to what is observed in Fig. 3 and 4, a battery material exhibiting faradaic reactions would have a nonuniform current distribution whenever the potential distribution was nonuniform. For example, Newman and Tobias[17] solved for the steady-state current distribution in a porous electrode using Tafel kinetics. The dimensionless parameter for the total current in their analysis, δ, can be expressed in terms of I^* as

$$\delta = I^* \frac{V_o(1-\alpha)nF}{RT} \quad [27]$$

Assuming $\alpha = 0.5$ and $V_o = 0.5$

$$\delta \approx 10\, I^* \quad [28]$$

Therefore, an $I^* = 1.0$ is roughly equivalent to $\delta = 10$. From Fig. 2 in Newman and Tobais,[17] the reaction current is fifteen times greater at the front of the electrode compared to the back. A similar distribution is seen in Fig. 3, but at $\tau I^* > 0.4$, the current distribution varies across the electrode by less than 8%.

Figure 5 shows the effect of changing the ratio of the matrix to solution phase conductivity, γ on the constant current discharge. For a given I^*, as γ increases from 0.0 to 1.0 the resistance of the cell increases and this leads to three distinct effects: (*i*) an offset in the cell voltage at the start of discharge; (*ii*) a reduction in the curvature of the discharge profile at the start of the discharge; and (*iii*) a decrease in utilization as the matrix and solution-phase conductivities approach each other, seen for higher discharge rates. The offset in the voltage at the start of discharge is due to the increased resistance in the cell. The reduction in curvature occurs due to an increasingly uniform discharging of the electrode, as the matrix conductivity is lowered.[8] For low internal resistance, no drop in utilization is seen over the operating voltage regime, but, as the internal resistance increases not only does the voltage window reduce dramatically, but also a loss in utilization is observed. This loss is observed because the voltage window is not large enough for the discharge to reach an ideal double-layer discharge profile, i.e., a straight line. For low internal resistance, the system reaches this linear profile before V^* reaches zero. Note that varying the matrix-phase conductivity has the same effect on the discharge curves as varying the solution-phase conductivity (i.e., discharge curves at $\gamma = 0.1$ is equivalent to that at $\gamma = 10$).

Although changing γ from 0.0 to 1.0 has the same qualitative effect on the discharge curve as increasing I^*, the behavior inside the electrode is very different. This difference can be seen by comparing the distribution in the double-layer current in Fig. 3 ($\gamma = 0.0$) with those in Fig. 6 ($\gamma = 1.0$). When the matrix conductivity is large (i.e., $\gamma = 0.0$), the portion of the electrode closest to the separator discharges preferentially as compared to the other parts of the electrode (Fig. 3). When the matrix conductivity is comparable to that of the solution ($\gamma = 1.0$), the electrode discharges at both the front and back (Fig. 6). Consequently, the current reaches a more uniform distribution at shorter times. For example, the current distribution at $\tau I^* = 0.1$ in Fig. 6 is more uniform than the profile at $\tau I^* = 0.2$ in Fig. 3.

Although higher γ reduces the time to reach uniform currents throughout the porous electrode, it does not translate to higher energies. The increased resistance as γ increases results in an offset in the voltage at the start of the discharge. As the area under the voltage-time curve is proportional to the energy delivered by the cell, increasing γ leads to a decrease in energy. The effect of β and γ on the energy efficiency of a device is shown in Fig. 7 as a function of the dimensionless current. The energy efficiency of the device was calculated by integrating Eq. 15 with respect to τ to yield

$$E^* = I^* \int_0^{\tau_c} V^* d\tau = I^* \tau_c \left[1 - \frac{I^*}{3} - \frac{I^* \tau_c}{2} - \frac{\beta I^*}{2}\right] - 2I^{*2} \sum_{n=1}^{\infty} \frac{\left(\frac{(-1)^n \gamma}{(\gamma+1)} + \frac{1}{(\gamma+1)}\right)^2 \left[\exp\left(-n^2\pi^2\tau_c\right) - 1\right]}{n^4\pi^4} \quad [29]$$

where τ_c is the time taken to reach the cutoff voltage (taken as 0 V in this analysis). At low current densities, the porous electrode behaves like an ideal capacitor (i.e., 100% efficient) because the discharge is uniform throughout the electrode. As the current density increases, the double-layer current distribution is less uniform for a large fraction of the discharge, and consequently not all the energy stored in the device can be removed. At a given I^*, as β increases from 0 to ∞ or γ increases from 0 to 1, the energy efficiency of the cell decreases as the overall resistance of the cell increases.

The results in Fig. 7 can be replotted in dimensional form as energy vs. power (i.e., Ragone plot) for different thicknesses, as shown in Fig. 8. The energy density was determined by estimating the dimensionless energy of the device from Eq. 29, converting E^* to a dimensional quantity, and dividing by the mass of the cell. The cell mass consists of the two electrodes, the separator and the electrolyte, and was obtained using

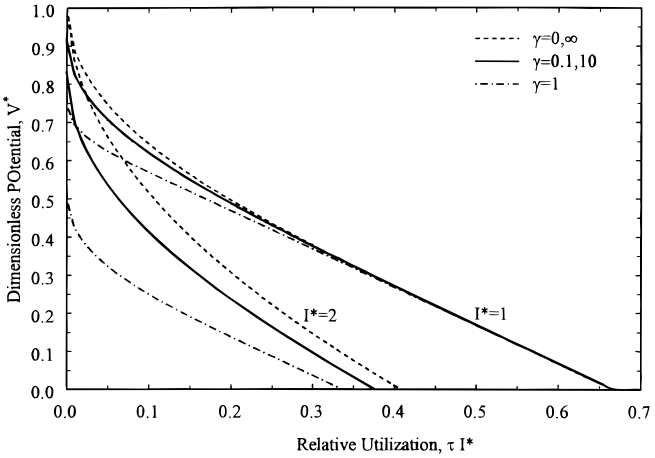

Figure 5. Normalized constant-current discharge curves as a function of the dimensionless current for an EC. At each current, the ratio of solution to matrix phase conductivity, γ, is varied. The separator resistance is negligible compared to that of the electrode (i.e., $\beta = 0$).

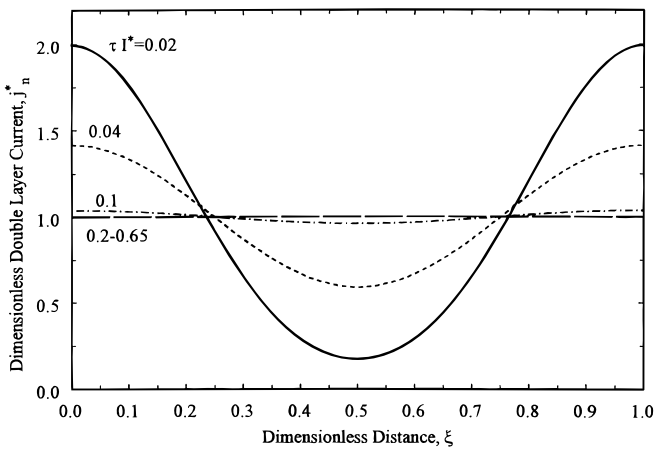

Figure 6. Double-layer current density distribution through the positive electrode as a function of time during constant-current discharge of an EC for $I^* = 1.0$. The conductivity of the matrix and solution phases are equal (i.e., $\gamma = 1$).

S0013-4651(98)08-081-1 CCC: $7.00

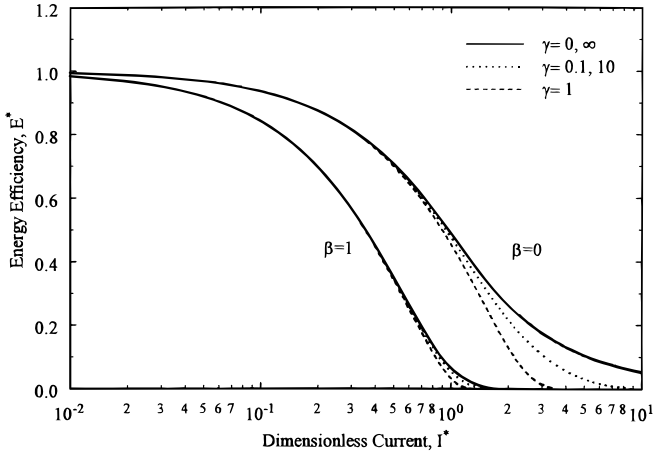

Figure 7. Dimensionless energy efficiency as a function of current for an EC. The graph was generated using Eq. 29. The solid line corresponds to $\gamma = 0$ or ∞, the dotted line to $\gamma = 0.1$ or 10, and the dashed line to $\gamma = 1.0$.

$$m = 2LA\rho_{\text{electrode}} + L_sA\rho_{\text{separator}} + 2\epsilon_oLA\rho_{\text{electrolyte}} + \epsilon_sL_sA\rho_{\text{electrolyte}} \quad [30]$$

The effective conductivity of the electrolyte in the electrode and in the separator was estimated using the correlation[18]

$$\kappa = \kappa_o\epsilon^{1.5} \quad [31]$$

The average power density was estimated by dividing the energy by the cutoff time, τ_c, and the weight of the device using Eq. 30. Although the power is the abscissa in Fig. 8, the current is the independent variable in this analysis.

Figure 8 is characterized by three distinguishing features: (*i*) at low currents (i.e., low power), thicker electrodes lead to higher energy densities, (*ii*) at high currents (i.e., high power) thinner electrodes leads to higher energy densities, and (*iii*) a maximum in the power density which results in two possible energy densities for every power density. This latter feature results from current being the independent variable. As the power is defined as the average voltage times the current, it is possible to achieve two energy densities with the same power density, one at low currents and thereby higher voltages and the other at high currents and consequently lower voltages. As the thickness of the electrode is increased, the fraction of the total device mass occupied by the two electrodes increases, and thus the energy density increases. In other words, the separator, which has no energy capacity, occupies a lower fraction of the overall mass. However, as the thickness of the electrode increases, the inefficiencies due to nonuniform charging of the electrode increase. These inefficiencies are more pronounced at higher currents, and consequently the energy density of the thicker electrode is less than that of the thinner one.

The energy of the device is limited by the potential window of operation, taken to be 1 V in this analysis for the aqueous electrolyte. The energy of the device can be increased considerably by using organic electrolytes, where the potential window is typically 4 V. As the energy of a capacitor scales as the square of the voltage, a fourfold increase in voltage results in a sixteen-fold increase in the energy. However, organic electrolytes can be an order of magnitude less conductive than aqueous systems.[19] This decreased conductivity leads to greater inefficiencies at higher currents. For example, in Fig. 7, if we consider a aqueous EC with $\beta = 0$ and $\gamma = 0$ operated at a current such that $I^* = 0.1$, then the device would be 100% utilized. By shifting to an organic electrolyte and operating at the same current, I^* increases by an order of magnitude (since I^* is inversely proportional to the conductivity), thus making the device 50% efficient. Thus, a trade-off exists between the energy and power capability of the device based on the choice of electrolyte.

Figure 9 shows the plot of energy density vs. the power density with the corresponding temperature rise at the end of discharge for electrodes of two thicknesses. The energy-density curves denoted by the solid lines are reproduced from Fig. 8. The temperature of the cell was estimated using Eq. 21 and represents the temperature at the end of the discharge. The dashed-dotted lines show the temperature at the end of discharge of a cell with finite external heat transfer from the cell, and the dashed line for adiabatic operation. At low power densities, the temperature rise is negligible initially as a consequence of the negligible ohmic loss. As the power density increases, the ohmic losses are such that an increase in temperature is observed. The temperature of the cell goes through a maximum with increasing power density since the utilization of the cell is very small at high power. The temperature increase in the cell is directly proportional to the ohmic loss in the cell, i.e., the voltage deviation from that of an ideal capacitor. As the power density increases, the electrode utilization reduces, and consequently the temperature increases. This is seen clearly by comparing the energy density curves and the temperature curves, i.e., an energy density decrease corresponds to a temperature increase. At very high power densities, the cell discharges for a very short time, and consequently the temperature increase is not appreciable. Thus, the temperature rise goes through a maximum after which it drops back to the ambient temperature of

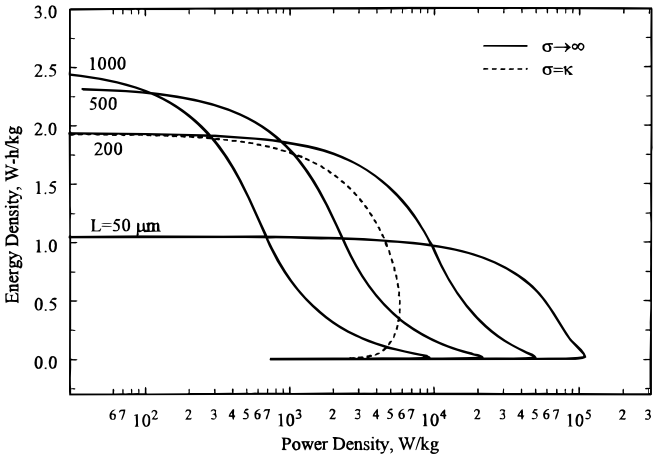

Figure 8. Energy density as a function of average power density for various electrode thicknesses. The solid line corresponds to $\gamma = 0$ or ∞, and the dashed line to $\gamma = 1$. The physical parameters used to generate the plot are listed in Table I.

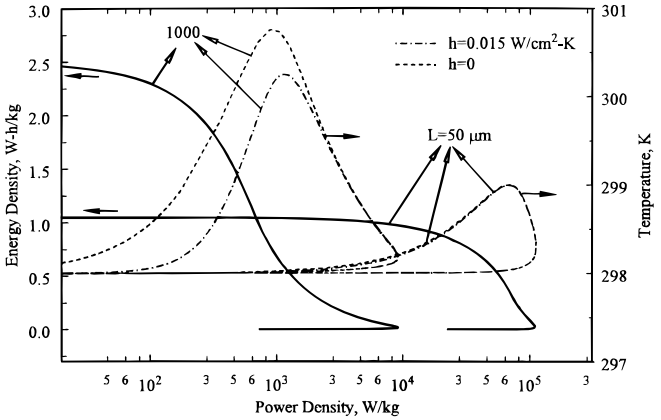

Figure 9. Energy density and temperature vs. power density for various electrode thicknesses. The solid lines are reproduced from Fig. 8. The dashed line corresponds to the temperature with no external heat transfer, and the dashed-dotted line to the temperature with external heat transfer. The physical parameters used to generate the plot are listed in Table I.

S0013-4651(98)08-081-1 CCC: $7.00

the cell. This phenomenon is observed in all the curves, with or without external heat transfer. When the device is operated adiabatically, the nature of the curves remain the same, but the temperature rise occurs at a lower power density, and the maximum temperature is higher. This effect is more prominent for thicker electrodes, since the temperature rise is greater in these cells. The choice of electrolyte would also play a crucial role in the temperature increase in the cell. Organic electrolytes increase the voltage window, thereby increasing the time of discharge (and consequently, the time for the heat to build up). In addition, the poor conductivity of the electrolytes increases the inefficiency at high currents, thus increasing the driving force for heat generation.

Although the maximum temperature rise in the device does not exceed a few degrees in the one cycle shown in Fig. 9, the temperature rise could be significant over a number of successive charge-discharge cycles. Figure 10 shows the temperature rise of the device as a function of the cycle number, for a capacitor with 50 μm electrodes operated at ca. 35 kW/kg specific power. The temperature of the device was calculated using Eq. 21 at the end of each half cycle. The dotted line in Fig. 10 shows the temperature rise for a capacitor operated adiabatically where the conductivity of the electrolyte is constant. The temperature rise in this cell is a constant and scales with the cycle number. The dashed line denotes the temperature rise when the temperature dependence on the conductivity is incorporated using[20]

$$\kappa = K_1T + K_2T^2 + K_3M + K_4M^2 + K_5TM + K_6MT^{-1} + K_7M^3 + K_8T^2M^2 \quad [32]$$

Due to the negligible change in temperature during a half cycle, the conductivity was assumed constant during the half cycle, but allowed to vary between half cycles. When the temperature increases, the conductivity of KOH increases, and thus the electrode utilization increases (see Fig. 2). This leads to lower ohmic losses in the cell, and the temperature rise gradually becomes less as the temperature increases, leading the plot to deviate from that for constant κ. The solid lines in the graph denote temperature rises with external heat transfer. As expected, the temperature rise at the initial cycles is similar for all the five cases. As the temperature increases, the rate of the external heat transfer increases, and the temperature reaches a steady-state value depending on the value of *h*, the external heat-transfer coefficient.

Impedance spectroscopy.—Figure 11 shows the dimensionless Nyquist plot of a porous, double-layer capacitor cell as a function of

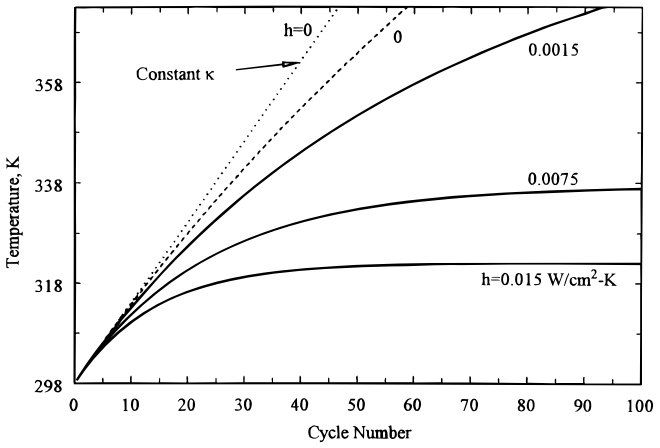

Figure 10. Temperature as a function of cycle number during continuous cycling of an EC. The solid line denotes finite external heat transfer, and the dashed and dotted lines for adiabatic operation. The dotted line is for constant electrolyte conductivity. The curves were generated for an electrode thickness of 50 μm, and the value for the physical parameters listed in Table III at a power density of 35 kW/kg.

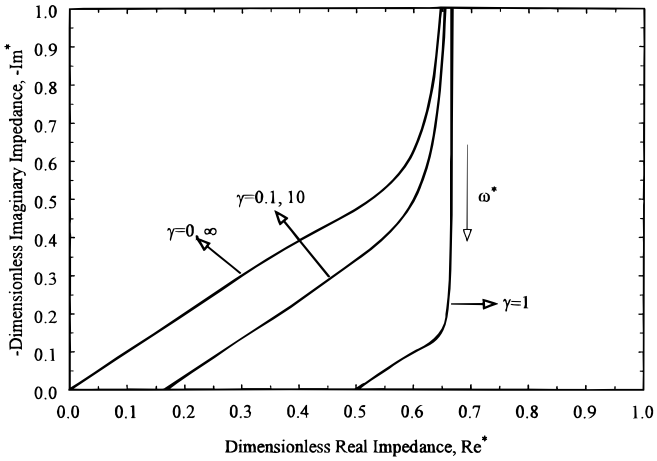

Figure 11. Simulated dimensionless Nyquist plot of an EC as a function γ. The graph was generated using Eq. 24 for β = 0.

the ratio of the solution to matrix conductivities. The graph was generated for negligible separator resistance (i.e., β = 0) using Eq. 24a and b. The graph shows three regions: (*i*) an initial ca. 45° line at high frequencies that intersects the real-axis at a finite value, (*ii*) an almost vertical line at very low frequencies, and (*iii*) a transition region where the slope shifts from 1 to infinity. Therefore, a slope of 2 is a convenient definition for the transition point between the two frequency limits.[21] These three regions are evident regardless of the value of γ. The only effect of γ on the impedance curve is that the high-frequency limit increases as γ increases from 0 to 1 (or γ decreases from ∞ to 1). The Nyquist plot also retains the shape shown in Fig. 11 as the separator resistance (i.e., β) increases. Examining Eq. 24a and b reveals that β has no effect on the imaginary component of the impedance, and the real component is shifted by a constant amount equal to β at all frequencies.

The effect of γ and β on the Nyquist plot can also be seen by examining the high- and low-frequency limits of Eq. 24a. As ω* approaches infinity, Eq. 24a reduces to

$$Re^* = \frac{2\gamma}{(1+\gamma)^2} + \beta \quad [33]$$

and as ω* approaches zero, Eq. 24a reduces to

$$Re^* = \frac{2}{3} + \beta \quad [34]$$

Again, only the high-frequency limit is affected by γ, but both limits are affected equally by β. Equations 33 and 34 are consistent with the short-time and long-time voltage offsets determined using the constant-current model (i.e., Eq. 25 and 26), respectively. The first term in Eq. 33 is the equivalent resistance of two resistors connected in parallel, one corresponding to the metal, and the other to the solution. From Fig. 3 it is clear that at short times and high matrix conductivity (i.e., γ = 0), the currents travels predominantly through the matrix phase. Therefore, at γ = 0 and high frequencies, the cell resistance is mainly due to the separator. When the matrix and solution conductivities are comparable (i.e., γ = 1), the transfer of current occurs at both the front and back ends (see Fig. 6), and the current is split between the matrix and the solution phases. Therefore, at γ = 1 and at high frequencies, the cell resistance is due to the separator and the porous electrodes. At long times (or low frequencies), the cell behaves like an ideal capacitor with three resistors in series, one each corresponding to the separator, matrix, and solution. Therefore, the first term in Eq. 34, in dimensional form, is related to the sum of the matrix and solution resistances.

The Nyquist plot shown in Fig. 11 is similar to that observed for a system with a faradaic reaction in a finite volume limited by bulk diffusion.[16] This similarity arises from the nature of the governing

S0013-4651(98)08-081-1 CCC: $7.00

Table I. Parameters used in the simulations to generate Fig. 8, 9, 10, and 12. The symbol * indicates assumed values.

Parameter	Value	Ref.
a	3×10^6 cm^2/cm^3	Johnson and Newman[10]
C	30 μF/cm^2	Johnson and Newman[10]
L_S	100×10^{-4} cm	*
$2V_O$	1.0 V	*
ϵ_O	0.25	Johnson and Newman[10]
ϵ_S	0.7	*
κ_O	0.67 Ω^{-1} cm^{-1}	CRC handbook[22]
$\rho_{electrolyte}$	1.2528 g/cm^3	De Vidts et al.[23]
$\rho_{electrode}$	1.0 g/cm^3	Kirk-Othmer[24]
$\rho_{separator}$	0.95 g/cm^3	*
$c_{p,carbon}$	1.05 J/g-K	Kirk-Othmer[24]
$c_{p,sep}$	1.0 J/g-K	*
$c_{p,KOH}$	3.1404 J/g-K	De Vidts et al.[23]
h	0.015 W/cm^2-K	Verbrugge[25]

equations defining the two processes, namely, Fick's second law and Eq. 6. As indicated earlier, for $\gamma = 0$, Eq. 24a and b collapse to Eq. 10a, and b derived by Motupally et al.[16] Since the equations are identical, the dimensionless frequencies at a given ratio of imaginary vs. real (i.e., slope of curve in Fig. 11) are identical. For example, for both cases, the dimensionless frequency at which $Im^*/Re^* = 2.0$ is 3.2. The lone difference between these two sets of equations is the definition of the dimensionless frequency. The dimensionless frequency defined by Motupally et al.[16] is

$$\psi = \sqrt{\frac{2\omega l^2}{D}} \qquad [35]$$

Therefore, setting $\psi = 3.2$ and using values given by Motupally et al. of $l = 1$ μm and $D = 3.4 \times 10^{-8}$ cm^2/s (i.e., the value for proton diffusion in NiOOH), the transition occurs at a frequency of 2.7 Hz. The corresponding dimensionless frequency defined here is $2\omega^*$. Therefore, setting $2\omega^* = 3.2$, and using $\gamma = 0$, $L = 150$ μm, and values for a, C, and κ given in Table I, the transition occurs at a frequency of 3.3 Hz. Therefore, the transition region observed in the impedance response of a porous double-layer process and a bulk diffusion process could occur at comparable frequencies. In other words, differentiating between these two processes based on a Nyquist plot alone is not possible.

The impedance model can be manipulated to obtain a plot of the effective capacitance of the cell vs. the applied frequency for electrodes of various thicknesses. The result is plotted in Fig. 12. For a pure capacitor (i.e., no charge-transfer resistance), the capacitance is equal to the inverse of the frequency times the imaginary component of the frequency response.[4] Therefore, the capacitance was calculated using

$$C = \frac{\kappa\sigma}{Im^*\omega(\kappa + \sigma)L} \qquad [36]$$

where Im^* is obtained from Eq. 24b.

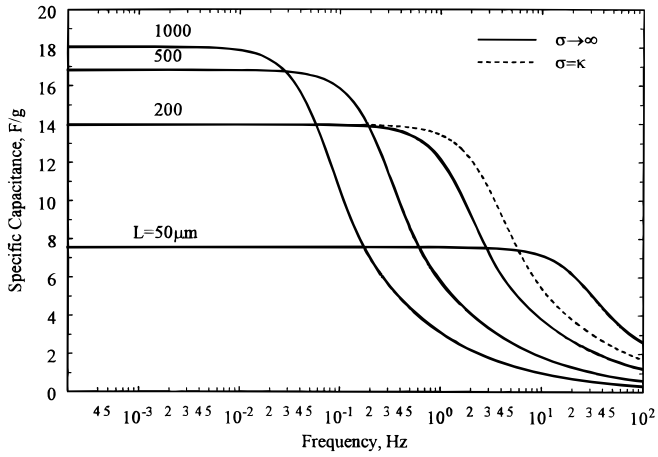

Figure 12. Effective capacitance as a function of frequency for an EC. The solid line corresponds to $\gamma = 0$ or ∞, and the dashed line to $\gamma = 1$. The graph was generated using the values listed in Table I.

Figure 12 is characterized by three distinguishing features: (*i*) at low frequency (i.e., low power) thicker electrodes lead to higher capacitance, (*ii*) at high frequencies (i.e., high power) thinner electrodes lead to higher capacitance, and (*iii*) at high frequencies lower matrix conductivity leads to higher capacitance. The capacitance has the same qualitative trend as the energy density vs. current (a dimensional form of Fig. 7). As the thickness of the electrode is increased, the fraction of the total device mass occupied by the two electrodes increases, and thus the capacitance increases. At high frequencies, nonuniform utilization of the double layer becomes more prominent for thicker electrodes, and the effective capacitance decreases with increasing electrode thicknesses. As the matrix-phase conductivity is lowered (i.e., $\gamma \rightarrow 1.0$), the current distribution throughout the porous electrode becomes more uniform. The more uniform the current distribution, the closer the impedance curve resembles an ideal capacitor. Therefore, at a given frequency, as γ increases from 0.0 to 1.0, the effective capacitance of the cell increases. However, higher effective capacitances do not necessarily lead to higher energies. For example, at $L = 200$ μm, the effective capacitance of the cell increases as the matrix conductivity decreases. However, in Fig. 7, the energy decreases as the matrix conductivity decreases because the increased cell resistance causes a decrease in the cell voltage.

Conclusion

A mathematical model was developed to simulate the performance of an electrochemical capacitor under two operating regimes: (*i*) constant-current discharge and (*ii*) electrochemical impedance spectroscopy. The constant-current discharge model was used to develop relationships to relate the physical properties (porosity, thickness, etc.) to performance (energy and power density). In addition, this model was used to estimate the heat generated in the device under various conditions and gauge its effect on continuous cycling. The model predicts the trade-off between energy and power density as the physical properties of the cell components are varied. Finally, the ac impedance behavior of the device was simulated as an electroanalytical tool to study more efficiently new materials in these novel devices.

Acknowledgments

The authors gratefully acknowledge the financial support from the U.S. Department of Energy under Cooperative Agreement No. DE-FC02-91ER75666.

The University of South Carolina assisted in meeting the publication costs of this article.

List of Symbols

a	interfacial area per unit volume, cm^2/cm^3
A	cross-sectional area of the electrode, cm^2
A_C	surface area of the cell, cm^2
C	capacitance per interfacial area, F/cm^2
C_P^*	dimensionless specific heat capacity of the cell ($mC_pT_O/V_O^2 AaCL$)
C_P	specific heat capacity of the cell, J/g-K
$c_{p,carbon}$	specific heat capacity of carbon, J/g-K
$c_{p,KOH}$	specific heat capacity of electrolyte, J/g-K
$c_{p,separator}$	specific heat capacity of separator, J/g-K
D	diffusion coefficient, cm^2/s
E^*	dimensionless energy ($E/2aCLV_o^2$)
E	energy, J/cm^2
F	Faradays constant, 96,487 C/equiv
h	external heat-transfer coefficient, W/ cm^2-K
h^*	dimensionless external heat-transfer coefficient (hA_CT_S/V_OIA)
I	cell current density, A/cm^2
I^*	dimensionless cell current $[IL(\kappa + \sigma)/\kappa\sigma V_O]$

S0013-4651(98)08-081-1 CCC: $7.00

i_1	current per cross-sectional area in the matrix phase, A/cm^2
i_2	current per cross-sectional area in the solution phase, A/cm^2
i_n	double-layer current per interfacial area, A/cm^2
Im	imaginary impedance, Ω cm^2
Im^*	dimensionless imaginary impedance $[Im\kappa\sigma/L(\kappa + \sigma)]$
j	imaginary number, $\sqrt{-1}$
j_n^*	dimensionless double-layer current $(-i_n aL/I)$
K_1-K_8	constants to calculate conductivity (see Ref. 20)
L	thickness of the electrode, cm
L_S	thickness of the separator, cm
l	diffusion length, cm
M	molarity of KOH, M
m	mass of the cell, kg
n	number of electrons transferred
R	universal gas constant, 8.3143 J/K-mol
Re	real impedance, Ω cm^2
Re^*	dimensionless real impedance $[Re\kappa\sigma/L(\kappa + \sigma)]$
s	dimensionless Laplace operator
T	temperature of the cell, K
T_O	initial temperature of the cell, K
T_S	ambient temperature of the surroundings, K
t	time, s
V^*	dimensionless cell voltage $(V_{cell}/2V_0)$
V_{cell}	cell voltage on discharge, V
V_0	initial single-electrode voltage on discharge, V
x	distance, cm
Z	complex impedance, Ω cm^2
Z^*	dimensionless complex impedance $[Z\kappa\sigma/L(\kappa + \sigma)]$

Greek

α	transfer coefficient
β	ratio of separator to electrode resistance $[L_S\kappa\sigma/\kappa_S L(\kappa + \sigma)]$
δ	dimensionless current $[I^*V_o(1 - \alpha)nF/RT]$
ϵ_O	porosity of the electrode
ϵ_s	porosity of the separator
ϕ_1	matrix phase potential, V
ϕ_2	solution phase potential, V
γ	ratio of solution to matrix phase conductivity (κ/σ)
η^*	overpotential $(\phi_1 - \phi_2/V_O)$
κ_o	bulk conductivity of the electrolyte, Ω^{-1} cm^{-1}
κ	effective conductivity of the electrolyte in the electrode, Ω^{-1} cm^{-1}
κ_s	effective conductivity of the electrolyte in the separator, Ω^{-1} cm^{-1}
λ	ratio of ambient temperature to initial cell temperature (T_S/T_O)
$\rho_{electrode}$	density of the electrode material, g/cm^3
$\rho_{electrolyte}$	density of the electrolyte, g/cm^3
$\rho_{separator}$	density of the separator material, g/cm^3
σ	matrix phase conductivity, Ω^{-1} cm^{-1}
τ	dimensionless time $[t\kappa\sigma/aCL^2(\kappa + \sigma)]$
ω	angular frequency, (s^{-1})
ω^*	dimensionless angular frequency $\left(\sqrt{\omega aCL^2(\kappa + \sigma)/2\kappa\sigma}\right)$
ξ	dimensionless distance (x/L)
ψ	$\sqrt{2\omega l^2/D}$

References

1. B. E. Conway, *J. Electrochem. Soc,* **138,** 1539 (1991).
2. S. Trasatti and P. Kurzweil, *Platinum Met. Rev.,* **38,** 46 (1994).
3. S. Sarangapani, B. V. Tilak, and C.-P. Chen, *J. Electrochem. Soc*, **143**, 3791 (1996).
4. A. J. Bard and L. R. Faulkner, *Electrochemical Methods: Fundamentals and Applications*, John Wiley & Sons Inc., New York (1980).
5. S. T. Mayer, R. W. Pekala, and J. L. Kaschmitter, *J. Electrochem. Soc,* **140**, 446 (1993).
6. K. C. Liu and M. A. Anderson, *J. Electrochem. Soc.*, **143**, 124 (1996).
7. V. Srinivasan and J. W. Weidner, *J. Electrochem. Soc.*, **144**, L210 (1997).
8. C. J. Farahmandi, in *Proceedings of the Symposium on Electrochemical Capacitors II*, F. M. Delnick, D. Ingersoll, X. Andrieu, and K. Naoi, Editors, PV 96-25, p. 167, The Electrochemical Society Proceedings Series, Pennington, NJ (1997).
9. F. A. Posey and T. Morozumi, *J. Electrochem. Soc.*, **113**, 176 (1966).
10. A. M. Johnson and J. Newman, *J. Electrochem. Soc.*, **118,** 510 (1971).
11. W. Tiedemann and J. Newman, *J. Electrochem. Soc.*, **112**, 70 (1975).
12. L. G. Austin and E. G. Gagnon, *J. Electrochem. Soc*, **120**, 251 (1973).
13. E. G. Gagnon, *J. Electrochem. Soc.*, **121**, 512 (1974).
14. B. Pillay and J. Newman, *J. Electrochem. Soc.*, **143**, 1806 (1996).
15. J. R. Miller, in *Proceedings of the Symposium on Electrochemical Capacitors*, F. M. Delnick and M. Tomkiewicz, Editors, PV 95-29, p. 246, The Electrochemical Society Proceedings Series, Pennington, NJ (1995).
16. S. Motupally, C. C. Streinz, and J. W. Weidner, *J. Electrochem. Soc.*, **142**, 1401 (1995).
17. J. S. Newman and C. W. Tobias, *J. Electrochem. Soc.*, **109**, 1183 (1962).
18. J. Newman, *Electrochemical Systems*, Prentice-Hall, Inc., Englewood Cliffs, NJ (1973).
19. M. Ue, K. Ida, and S. Mori, *J. Electrochem. Soc.*, **141**, 2989 (1994).
20. D. See and R. E. White, *J. Chem. Eng. Data.*, **42**, 1266 (1997).
21. R. D. Armstrong, *J. Electroanal. Chem.*, **198**, 177 (1986).
22. *CRC Handbook of Chemistry and Physics*, 53rd ed., R. C. Weast, Editor, CRC Press Inc., Boca Raton, FL (1979).
23. P. De Vidts, J. Delgado, and R. E. White, *J. Electrochem. Soc.*, **142**, 4006 (1995).
24. *Kirk-Othmer Encyclopedia of Chemical Technology,* Vol. 4, 4th ed., John Wiley & Sons, New York (1992).
25. M. W. Verbrugge, *AIChE J.*, **41**, 1550 (1995).